NASA
Technical Memorandum 107432

Army Research Laboratory
Technical Report ARL–TR–1355

Microfabricated Ice-Detection Sensor

Russell G. DeAnna
U.S. Army Research Laboratory
Lewis Research Center
Cleveland, Ohio

Mehran Mehregany and Shuvo Roy
Case Western Reserve University
Cleveland, Ohio

Prepared for the
Smart Structures and Materials Conference
sponsored by the Society for Photo-Optical Instrumentation Engineers
San Diego, California, March 2–6, 1997

National Aeronautics and
Space Administration

U.S. ARMY
RESEARCH LABORATORY

Microfabricated ice-detection sensor

Russell G. DeAnna [a] , Mehran Mehregany [b] , Shuvo Roy [b] , and Eugene Zakar [c]

[a] Vehicle Technology Center, US Army Research Laboratory, NASA Lewis Research Center, Cleveland, OH 44135

[b] Microfabrication Laboratory, Department of Electrical Engineering & Applied Physics, Case Western Reserve University, Cleveland, OH 44106

[c] Sensors and Electron Devices Directorate, US Army Research Laboratory, Ft. Monmouth, NJ, 07703

ABSTRACT

Knowledge of ice conditions on important aircraft lift and control surfaces is critical for safe operation. These conditions can be determined with conventional ice-detection sensors, but these sensors are often expensive, require elaborate installation procedures, and interrupt the airflow. A micromachined, silicon-based, flush-mounted sensor which generates no internal heat has been designed, batch fabricated, packaged, and tested. The sensor is capable of distinguishing between an ice-covered and a clean surface. It employs a bulk micromachined wafer with a 7μm-thick, boron-doped, silicon diaphragm which serves as one plate of a parallel-plate capacitor. This is bonded to a second silicon wafer which contains the fixed electrodes -- one to drive the diaphragm by application of a voltage, the other to measure the deflection by a change in capacitance. The diaphragm sizes ranged from 1x1mm to 3x3mm, and the gap between parallel-plate capacitors is 2μm. A 200V d.c. was applied to the driving electrode which caused the capacitance to increase approximately 0.6pf -- from a nominal capacitance of 0.6pf -- when the surface was ice free. After the sensor was cooled below the freezing point of water, the same voltage range was applied to the drive electrode. The capacitance increased by the same amount. Then a drop of water was placed over the diaphragm and allowed to freeze. This created an approximately 2mm-thick ice layer. The applied 200V d.c. produced no change in capacitance, confirming that the diaphragm was locked to the ice layer. Since the sensor uses capacitive actuation, it uses very little power and is an ideal candidate for inclusion in a wireless sensing system.

Keywords: ice detection, icing, sensors, microfabricated, MEMS, diaphragm, capacitive sensors

1. INTRODUCTION

Since the first aircraft flights during winter, icing has been recognized as a potentially dangerous phenomenon. Numerous aircraft accidents have occurred due to icing, and ice detection must occur before ice removal. In the air, icing is caused by super-cooled water droplets in clouds, which are in a metastable condition. The droplets follow trajectories which will either strike the surface, or will be carried away from it. When the aircraft encounters these droplets, they may either suddenly change phase upon impact, or may flow back as a thin film of water and collect into droplets due to surface tension. The droplets may be swept off the surface by aerodynamic forces or freeze. The temperature range normally associated with icing is from -40 to 0 C.

Various technologies have been used to detect ice. For a detailed account of these detection techniques and other icing-related issues consult the FAA handbook.[1] Microwave and other electro-mechanical techniques have been used for both point and area detection.[2-5] Vibrating probes and diaphragms which change characteristics when ice covered have been used for point dection.[6,7]

2. SENSOR DESIGN

A schematic, cross-sectional view of the ice-detection sensor is shown in Fig. 1. There are two aluminum electrodes patterned on the Pyrex wafer and located under the diaphragm. The outside electrode is used to sense diaphragm deflection upon applied voltage to the drive, or inner, electrode.

There is a silicon diaphragm bonded to the Pyrex substrate which acts as a third electrode, electrically isolated from the two aluminum electrodes. By keeping the diaphragm at a constant potential and applying a voltage on the drive electrode, an attractive force will be induced between the two, causing the diaphragm to deflect toward the substrate. This deflection will cause an increase in capacitance between the sensing electrode and the diaphragm. Although not shown in the figure, air-release channels are included between the sealed region under the diaphragm and the edge of the chip. This allows the pressure underneath the diaphragm to equalize with the ambient air outside the diaphragm, and allows reduction of air damping on the membrane if an alternating voltage were used to drive the diaphragm. The sensor is designed to operate with a d.c. voltage; the size and thickness of the diaphragm are such that resonance or oscillatory motion are precluded. (Though a resonant diaphragm would allow measurement of various ice thicknesses by detection of the change in resonant frequency. This operating mode is currently under investigation and will be reported on in a subsequent paper.)

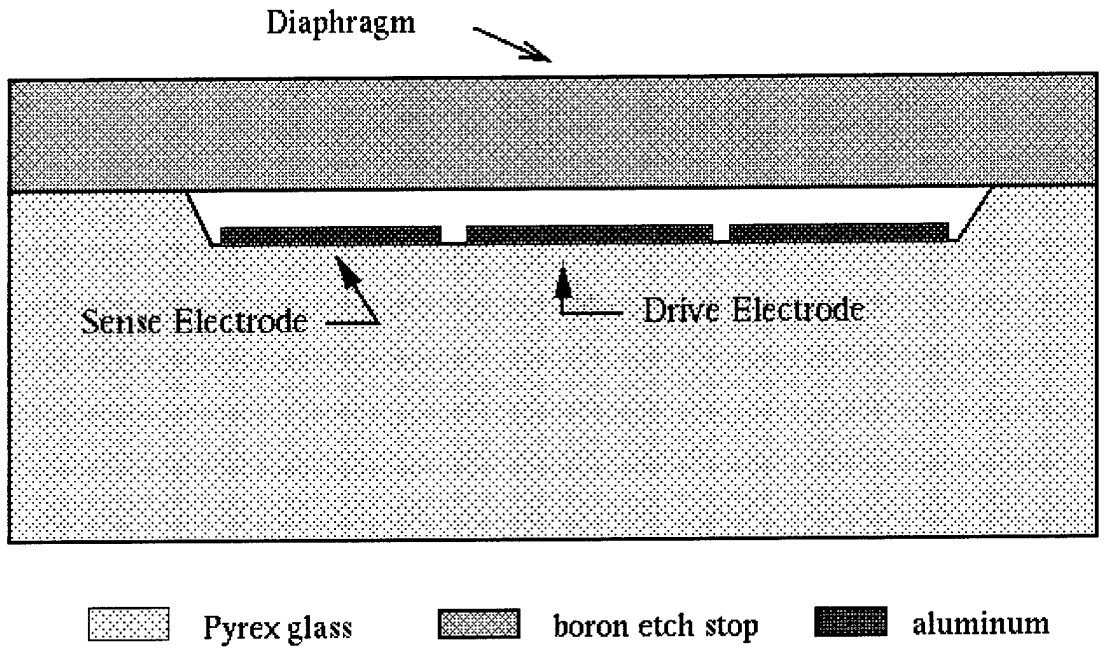

Figure 1: Sensor schematic cross section.

The capacitance and actuation voltages necessary to deflect the diaphragm depend strongly on the distance between the diaphragm and electrodes, and also on the diaphragm area. A larger diaphragm has a larger capacitance and requires a smaller actuation voltage, but is mechanically less robust and is also more sensitive to fluctuations in air pressure. Typical diaphragm dimensions are 1mm by 1mm square, 7μm thick, suspended 2μm above the electrodes. These dimensions yield a nominal capacitance of approximately 0.6pf between the diaphragm and either electrode. The electrodes have equal areas. The sensor is designed to operate with a 5 to 20V d.c. signal applied to the drive electrode. This should yield a capacitance change of a fraction of a picofarad. See Fig. 2 for a plan view SEM picture of the electrodes.

Three contact pads are provided per die (though only the two which provide electrical connections to the electrodes under the diaphragm can be seen in Fig. 2). The third contact pad provides electrical connection to the silicon substrate. The contact to the silicon substrate is through an aluminum line that crosses over the shallow etch step in the glass wafer and is then sandwiched between the glass and silicon wafer. Since the surface of the silicon wafer is doped very heavily with boron, the aluminum contact to the silicon will be ohmic. Each contact pad has an area of 250x250μm. The contact pads are exposed through windows etched in the silicon wafer.

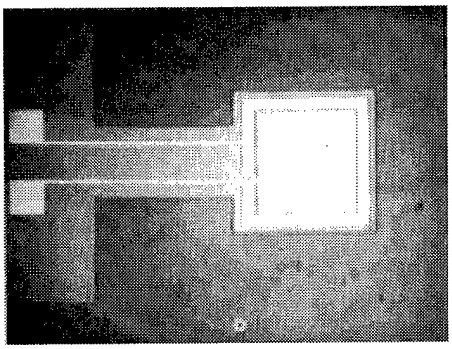

Figure 2: Plan view of aluminum electrodes.

Five diaphragm sizes – 1x1, 1x2, 1x3, 2x2, and 3x3mm -- were included on the mask layout. For each diaphragm size, the area of the two concentric electrodes under the diaphragm was equal, and each electrode has approximately one-half the area of the diaphragm. Thus, the electrode area, and not the diaphragm area, determines the electrode-to-diaphragm-capacitance magnitude. Two variations in the positioning of the channel through which the connections to the electrodes under the diaphragm are made were included. This was done to investigate the change in deflection for each type since the maximum stress location for a rectangular diaphragm with fixed edges is at the middle of each side. (See Fig. 9 in the results section, which shows the von-Mises strain computed from the FEA.) In the case that the channel connects the diaphragm area with the bonding pad area through the middle region of one of the diaphragm sides, the diaphragm mechanical response is expected to deviate more from the all-sides-fixed model than in the case when the channel is at the corner of one of the sides.

The deflection of the diaphragm with applied voltage can be estimated by assuming the diaphragm and electrodes form a pair of parallel-plate capacitors. The capacitance for such a configuration is given by

$$C = \varepsilon A / x, \tag{1}$$

where ε is the dielectric of the material between the plates, A is the plate area, and x is the gap between plates. For a 1x1mm diaphragm suspended 2μm above the electrodes, in air, the nominal capacitance is 0.6pf.[†] The capacitance change due to a change in gap spacing becomes

$$\Delta C = -\frac{\varepsilon A}{x^2}\Delta x. \tag{2}$$

This equation relates the capacitance change to diaphragm deflection, Δx. For a square plate clamped at the edges, the uniform pressure for a given maximum deflection is given by

$$p = -4.5E\left(\frac{t}{a}\right)^4 \frac{\Delta x_{max}}{t}, \tag{3}$$

which assumes no residual stress exists in the plate.[8] In this equation, t is the diaphragm thickness, a is one-half the diaphragm edge lentgth, p is pressure, and E is Young's Modulus. Solving the above equation for Δx_{max} gives

$$\Delta x_{max} = -\frac{tp}{4.5E}\left(\frac{a}{t}\right)^4. \tag{4}$$

For a voltage-driven plate, the pressure (load) is due to the applied voltage. For a parallel-plate capacitor the pressure for a given voltage is given by

[†] This assumes the drive and sense electrodes each occupy one-half the area of the diaphragm.

$$p = \frac{\varepsilon V^2}{2x^2}. \qquad (5)$$

Substituting this relation into the equation for maximum plate deflection gives

$$\Delta x_{max} = -\frac{\varepsilon t}{9Ex^2}\left(\frac{a}{t}\right)^4 V^2. \qquad (6)$$

This equation is used to verify the ANSYS FEA by comparing it with the center deflection computed by the model. For a square, silicon diaphragm in air of the dimensions given above, the center deflection becomes

$$\Delta x_{max} = 2.8x10^{-10} V^2 (m). \qquad (7)$$

An ANSYS finite-element model of this diaphragm is shown in Fig. 3. This model uses an array of 20x20x3, 8-node solid elements. In the FEA, a quarter of the diaphragm is modeled; symmetry boundary conditions are applied on two edges; and the other two edges have all their degrees-of-freedom fixed. To verify the FEA results, a pressure (see Eq. 5) corresponding to a 10V d.c. signal was applied to an electrode assumed to be equal in area to the entire diaphragm. Equation 7 yields a maximum deflection of 0.028μm. The FEA model computed a center deflection of 0.026μm. This is a good agreement and lends confidence to the FEA results where the actual electrode patterns are used to load the diaphragm.

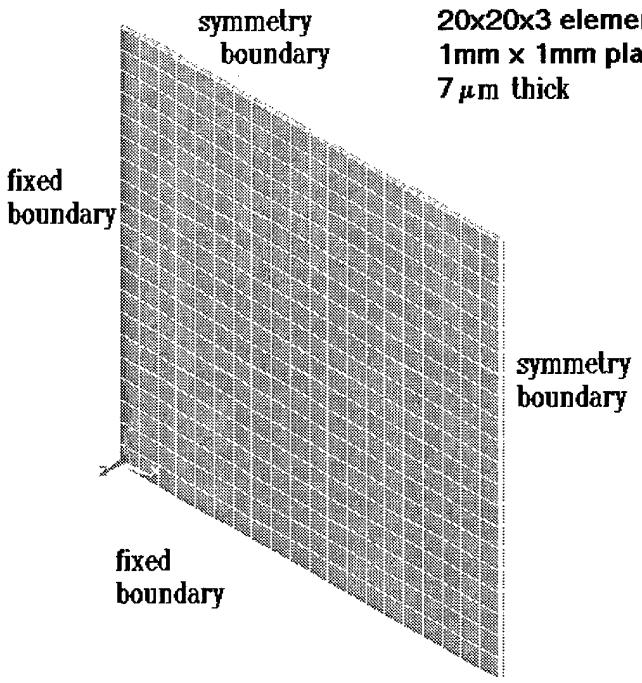

Figure 3: FEA grid.

3. SENSOR FABRICATION

The sensor is fabricated using anodic bonding between silicon and Pyrex glass. The two wafers are bonded together such that the drive and sense electrodes are underneath the diaphragm.. The fabrication process requires two masks associated with two photolithography steps. Starting with the glass substrate, the first mask is used to pattern a shallow recess area which will eventually form

the air gap between diaphragm and substrate and the access passages for aluminum interconnections. Standard (positive resist) lithography and an HF-based solution are used to create the recessed areas. Next, aluminum is deposited on the glass substrate by sputtering. The aluminum film is approximately 0.3μm thick. The aluminum is patterned with the second mask, using standard lithography and a wet aluminum etch.

The starting silicon wafer is oxidized thermally to grow a 1 μm-thick layer. The starting silicon wafer is (100), moderately doped n-type, double-sided polished, with a <100> major flat. Oxide on one surface is protected with hard-baked photoresist and the oxide on the opposite surface is removed in buffered HF. Next, the wafer is diffused with boron to create a boron etch stop layer, on the side with no oxide, with a thickness around 7μm. The boron-doped glass is removed in buffered HF.

The silicon wafer is electrostatically bonded to the glass wafer. The bonding step only requires good global alignment of the two wafers. The wafers are then etched in KOH, leaving behind the boron etch stop. The metal pads are sealed by the boron etch stop membrane. The pads are exposed by simply breaking away their corresponding diaphragms with a small vacuum probe. A cross-sectional SEM picture of the sensor is shown in Fig. 4. This figure shows both the diaphragm region and the region containing the passage for the aluminum interconnects for the electrodes.

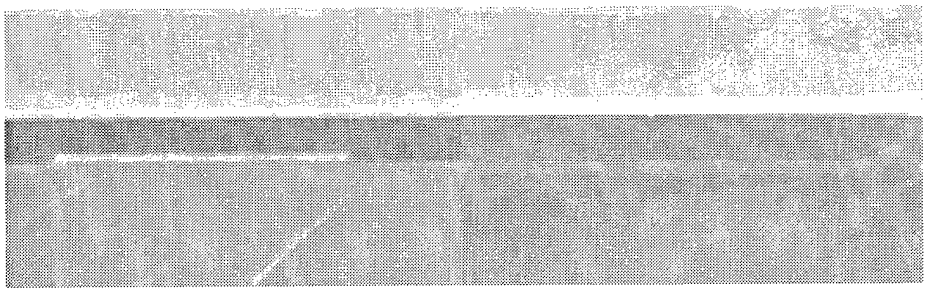

Figure 4: Sensor cross section.

After fabrication, the wafers were diced and each sensor was bonded to a ceramic substrate. Four sensors were mounted on each substrate. Wires were then bonded between gold leads on the substrate and the sensor's bonding pads. The wire bond locations were protected from mechanical loads and the icing environment by sealing them with epoxy. This epoxy also sealed the interconnect passage running under the diaphragm from the outside environment. This is necessary to prevent water or moisture from seeping in under the diaphragm or around the aluminum interconnects. Since water has an electrical dielectric which is approximately seventy times higher than air, care must be taken during testing so that moisture is prevented from accumulating on the connection points and causing erroneous data. The bonding of the silicon sensor to the ceramic substrate was done above room temperature. This caused a differential expansion between the silicon sensor and ceramic substrate which left a residual compression stress in the diaphragm, when the package was allowed to cool. This stress caused diaphragm buckling during some experiments. Often, the diaphragm would behave predictably the first time a voltage was applied, only to buckle at some higher voltage. Still other sensors behaved poorly from the start. In either case, it is clear that sensor packaging should be done carefully to avoid inducing more residual stress.

4. EXPERIMENTAL TESTING

The sensor was tested in the laboratory both with and without ice. The ceramic substrate, which contained four sensors, was placed on top of a block of frozen CO_2 and allowed to cool. Before ice was formed on the diaphragm, the sensor was tested to make sure the diaphragm was free to move. Then a drop of water was placed on the diaphragm. This drop froze within a few seconds. A photograph of the sensor covered by ice is shown in Fig. 5. The ice was approximately 2mm thick.

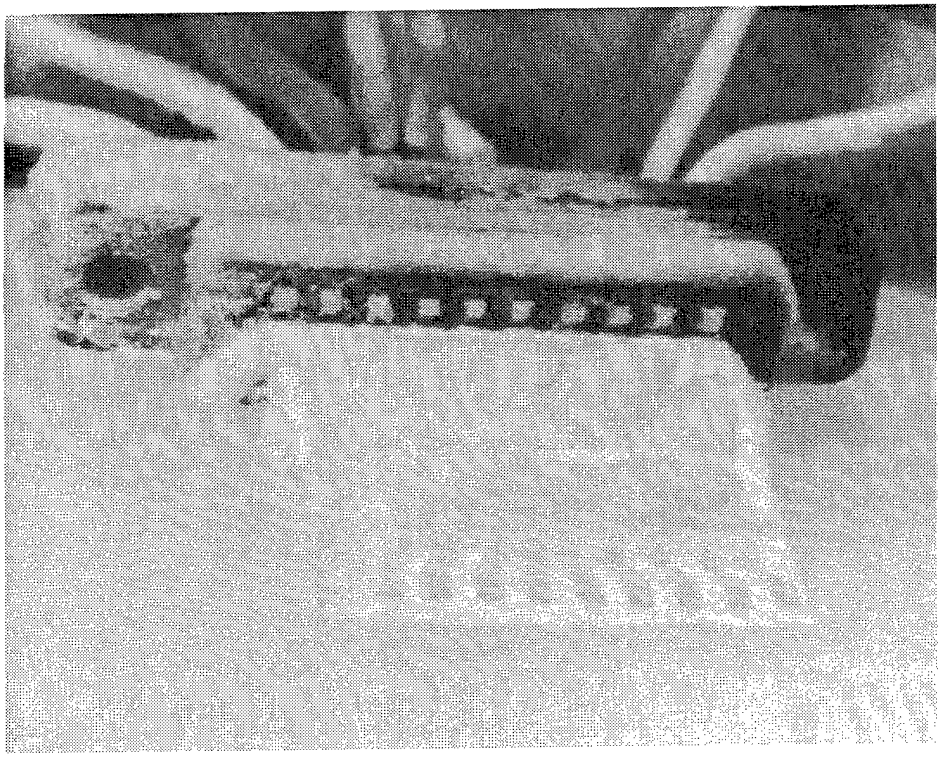

Figure 5: Ice-covered sensor.

A d.c. voltage was applied to the drive electrode through a large-magnitude resistor – typically 100 K ohms. The sense electrode was connected to the input of a frequency-modulated (FM) oscillator circuit which was used to measure the capacitance change. The FM oscillator has a nominal carrier frequency of 48MHz. The unit contains the FM oscillator, electronics and a signal conditioner. The signal conditioner demodulates the oscillator output. Capacitance change is registered as a change in the frequency of the demodulator. The oscillator frequency increases with increasing capacitance between diaphragm and sense electrode. See Fig. 6 for a circuit diagram.

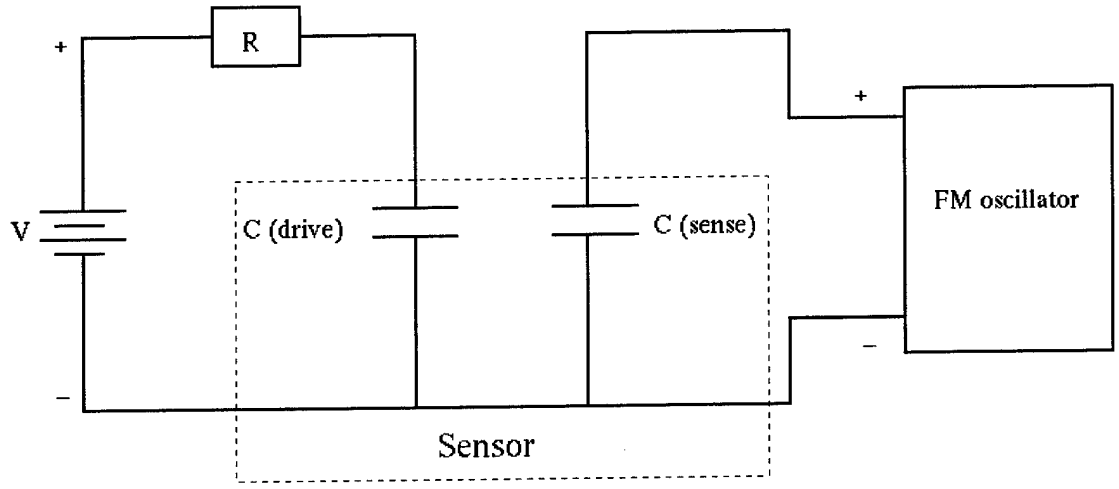

Figure 6: Circuit diagram for capacitance measurement.

The capacitance looking into the terminals can be thought of as the sum of the capacitance of the probe alone and the capacitance introduced by the sensor. The total capacitance as a function of applied voltage is

$$C(v) = C_0 + C_b(v), \tag{8}$$

where C_0 is the nominal circuit capacitance and $C_b(v)$ is the capacitance of the sensor. An important aspect of FM-oscillator design is the frequency of oscillation. The oscillating frequency without applied voltage, that is, when $C(0) = C_0 + C_b(0)$, is defined as the carrier frequency f_c, or

$$f_c = \frac{1}{2\pi}\sqrt{1/LC(0)}, \tag{9}$$

where L is the inductance of the inductor in the oscillator. The nominal frequency with zero applied voltage, f_c, is used to compute the nominal value of $LC(0)$. The nominal capacitance, $C_b(0)$, must be measured separately. The applied voltage causes a small change in the carrier frequency, defined as the frequency deviation Δf_c, found from

$$\Delta f_c = -[C_b(v) - C_b(0)]\frac{1}{4\pi C(0)}\sqrt{\frac{1}{LC(0)}}. \tag{10}$$

Rearranging gives the capacitance change as

$$C_b(v) - C_b(0) = 4\pi\Delta f_c C(0)\sqrt{LC(0)}, \tag{11}$$

which expresses the basic relationship between the capacitance change, as reflected in $C_b(v)$ and the quantities Δf_c, L, and $C(0)$. These quantities can then be used to compute the capacitance change for any applied voltage.

5. RESULTS

All of the experimental and theoretical results apply to a sensor with a diaphragm of 1x1mm area, 7μm -thick, suspended 2μm above the electrodes. Results were obtained both with and without ice. No attempt was made to detect ice thickness, and the goal was to yield either an ice or no-ice signal. No data were obtained with other ice thicknesses or temperatures.

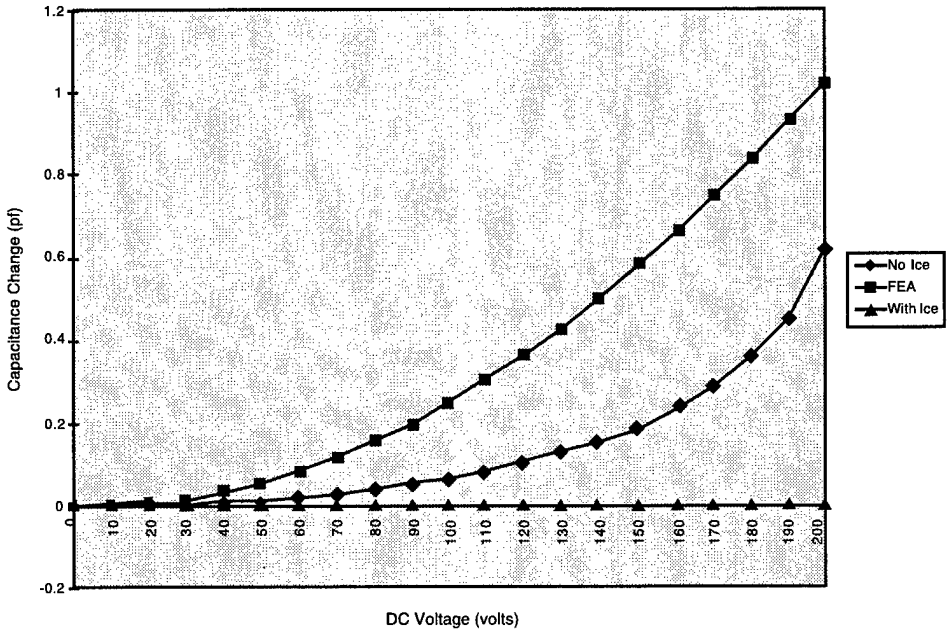

Figure 7: Capacitance change versus voltage.

Figure 7 shows capacitance change versus applied voltage for the experiment both with and without ice and for the ANSYS FEA without ice. In the FEA model a pressure, corresponding to a given voltage according to Eq. 5, was applied to the model over an area corresponding to the drive electrode (a 0.5x0.5mm area at the center of the diaphragm). The figure applies to a diaphragm without ice. There was no measurable difference in capacitance change between a room-temperature and cooled sensor when there was no ice covering the diaphragm. In the experiment, the capacitance change was measured directly by the signal-processing circuit; the capacitance change for the FEA was computed by numerically integrating the equation for capacitance change (Eq. 2) over the area represented by the sense electrode, i.e., that area outside of the 0.5x0.5mm area representing the drive electrode. The experimental capacitance change was approximately 60% less than the FEA. This difference is expected since the FEA doesn't consider residual stress or buckling. The maximum deflection from the FEA is 0.064μm. Figure 9 shows the computed von-Mises strain. It shows maximum strain at the center of each edge and minimum strain at the corners.

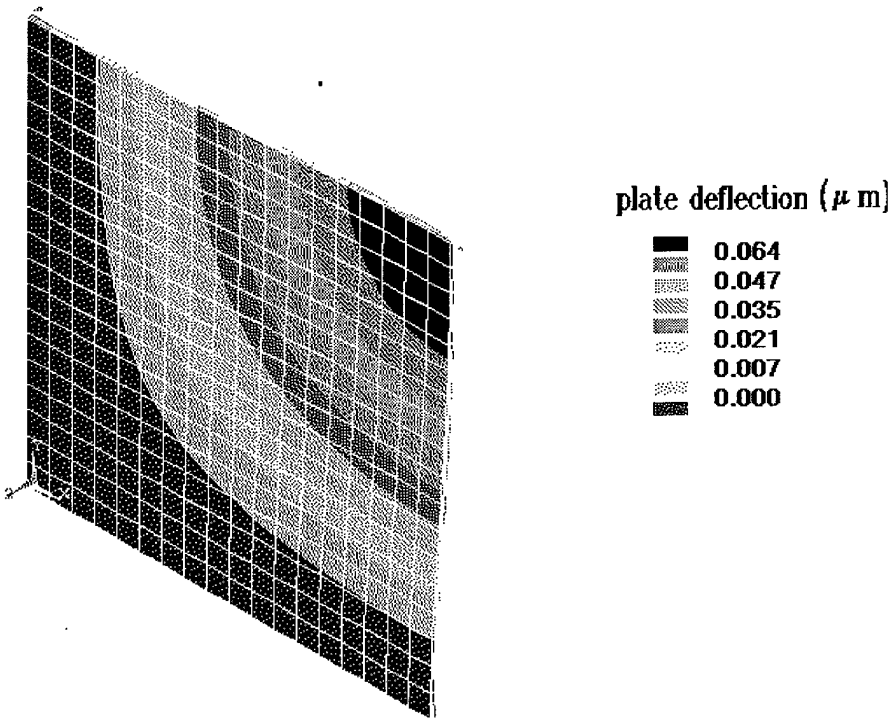

Figure 8: Diaphragm deflection.

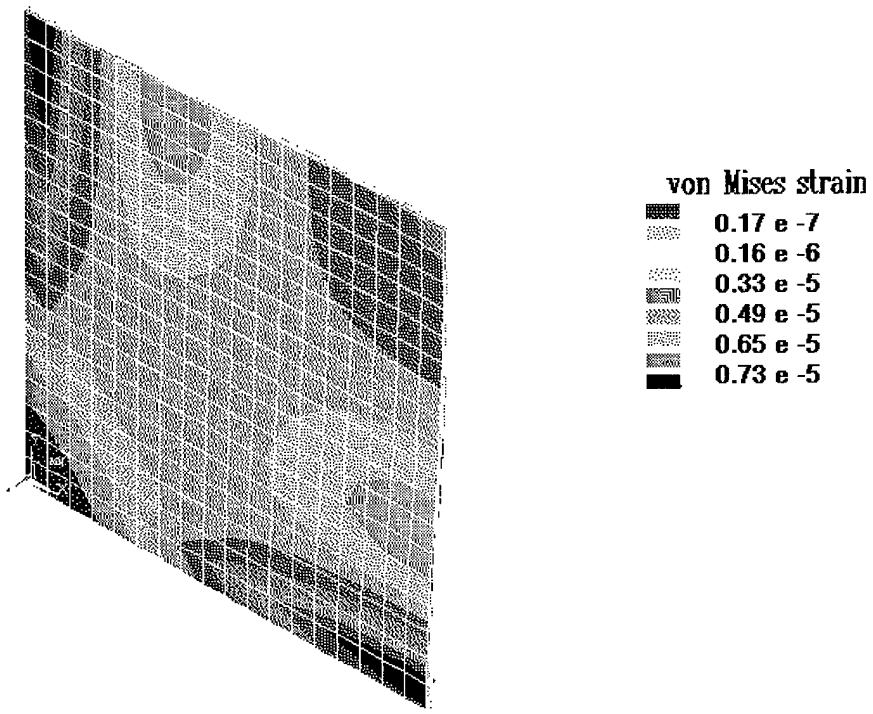

Figure 9: von-Mises strain.

When the sensor is covered by a 2mm-thick layer of ice, the applied voltage yields no diaphragm deflection as measured by the capacitance sensing circuit. Thus, the sensor is able to distinguish between ice and no ice.

6. CONCLUSION

The paper presents results which prove that a micromachined sensor using a silicon diaphragm suspended over a pair of electrodes used to drive and sense diaphragm deflection can be used to detect ice. The current batch of sensors could not be made to resonate because of packaging techniques and high residual stress levels which often led to diaphragm buckling. The current design has a diaphragm thickness which is also too thick for the diaphragm area to allow resonance. No data were taken with various ice thicknesses and ice temperatures. These data will be presented in a forthcoming paper which will include results from a new sensor design. The new design will also better protect the interconnects from the icing environment. This wasn't a problem in the current test since the sensor was operated in the ice or no-ice mode and the capacitance changes were easy to detect. But a sensor designed to measure ice thickness must not be sensitive to water or ice on the interconnects.

ACKNOWLEDGEMENTS

The ice sensor was designed by and mask layouts made by Advanced Micromachines Incorporated (AMMi) of Cleveland, Ohio. The work was supported by the Army Research Laboratory under contract number DAAL03-91-C—0034. The Case Western Reserve University work was supported by an Army Research Office MURI under contract number DAAH04-95-10097.

REFERENCES

1. Heinrich, A., et al., *Aircraft Icing Handbook*, Technical Center Publication DOT/FAA/CT-88/8-2, FAA, 1991.

2. Gerardi, J. J. and G. A. Hickman, "Distributed ice accretion sensor for smart aircraft structures," 27th AIAA Aerospace Sciences Meeting, Reno, NV, Jan. 9-12, 1989.

3. Deom, A. A. and J. C. Garnier, "Detection and measurement of ice accretion on a profile by an ultrasonic method," 25th AIAA Aerospace Sciences Meeting, Reno, NV, Jan. 12-15, 1987.

4. Hansman, R. J.and M. S. Kirby, "Measurement of ice accretion using ultrasonic pulse-echo techniques," 23rd AIAA Aerospace Sciences Meeting, Reno, NV, Jan. 14-17, 1985.

5. Magenheim, B. and J. K. Bocks, "Microwave ice accretion measurement instrument," 20th AIAA Aerospace Sciences Meeting, Orlando, FL, Jan. 11-14, 1982.

6. Jensen, D. P. And D. J. Moore, "An ice detection and control system for fixed and rotary wing aircraft," 8th Annual National Conference on Environmental Effects on Aircraft and Propulsion Systems, Bordentown, NJ, Oct. 8-10, 1968.

7. Lustenberger, M. "New ice detection system," Proceedings of the 14th Symposium on Aircraft Integrated Monitoring Systems, p. 619-638, Vibrometer, Fribourg, Switzerland, 1988.

8. Timoshenko, S., et al, *Theory of Plates and Shells*, p. 202, McGraw Hill, New York, 1959.

REPORT DOCUMENTATION PAGE

Form Approved
OMB No. 0704-0188

1. AGENCY USE ONLY (*Leave blank*)	2. REPORT DATE	3. REPORT TYPE AND DATES COVERED
	June 1997	Technical Memorandum

4. TITLE AND SUBTITLE

Microfabricated Ice–Detection Sensor

5. FUNDING NUMBERS

WU–523–26–13
1L161102AH45

6. AUTHOR(S)

Russell G. DeAnna, Mehran Mehregany, and Shuvo Roy

7. PERFORMING ORGANIZATION NAME(S) AND ADDRESS(ES)

NASA Lewis Research Center
Cleveland, Ohio 44135–3191
and
U.S. Army Research Laboratory
Cleveland, Ohio 44135–3191

8. PERFORMING ORGANIZATION REPORT NUMBER

E–10690

9. SPONSORING/MONITORING AGENCY NAME(S) AND ADDRESS(ES)

National Aeronautics and Space Administration
Washington, DC 20546–0001
and
U.S. Army Research Laboratory
Adelphi, Maryland 20783–1145

10. SPONSORING/MONITORING AGENCY REPORT NUMBER

NASA TM–107432
ARL–TR–1355

11. SUPPLEMENTARY NOTES

Prepared for the Smart Structures and Materials Conference sponsored by the Society for Photo-Optical Instrumentation Engineers, San Deigo, California, March 2–6, 1997. Russell G. DeAnna, U.S. Army Research Laboratory, NASA Lewis Research Center; Mehran Mehregany and Shuvo Roy, Case Western Reserve University, Cleveland, Ohio 44106. Responsible Person, Russell G. DeAnna, organization code 5610, (433–3385.

12a. DISTRIBUTION/AVAILABILITY STATEMENT

Unclassified - Unlimited
Subject Category 06

This publication is available from the NASA Center for AeroSpace Information, (301) 621–0390.

12b. DISTRIBUTION CODE

13. ABSTRACT ***(Maximum 200 words)***

Knowledge of ice conditions on important aircraft lift and control surfaces is critical for safe operation. These conditions can be determined with conventional ice-detection sensors, but these sensors are often expensive, require elaborate installation procedures, and interrupt the airflow. A micromachined, silicon-based, flush-mounted sensor which generates no internal heat has been designed, batch fabricated, packaged, and tested. The sensor is capable of distinguishing between an ice-covered and a clean surface. It employs a bulk micromachined wafer with a 7μm-thick, boron-doped, silicon diaphragm which serves as one plate of a parallel-plate capacitor. This is bonded to a second silicon wafer which contains the fixed electrodes — one to drive the diaphragm by application of a voltage, the other to measure the deflection by a change in capacitance. The diaphragm sizes ranged from 1x1mm to 3x3mm, and the gap between parallel-plate capacitors is 2μm. A 200V d.c. was applied to the driving electrode which caused the capacitance to increase approximately 0.6pf.— from a nominal capacitance of 0.6pf — when the surface was ice free. After the sensor was cooled below the freezing point of water, the same voltage range was applied to the drive electrode. The capacitance increased by the same amount. Then a drop of water was placed over the diaphragm and allowed to freeze. This created an approximately 2mm-thick ice layer. The applied 200V d.c. produced no change in capacitance, confirming that the diaphragm was locked to the ice layer. Since the sensor uses capacitive actuation, it uses very little power and is an ideal candidate for inclusion in a wireless sensing system.

14. SUBJECT TERMS

Ice detection; Icing; Sensors; Microfabricated; MEMS; Diaphragm; Capacitive sensors

15. NUMBER OF PAGES
12

16. PRICE CODE
A03

17. SECURITY CLASSIFICATION OF REPORT	18. SECURITY CLASSIFICATION OF THIS PAGE	19. SECURITY CLASSIFICATION OF ABSTRACT	20. LIMITATION OF ABSTRACT
Unclassified	Unclassified	Unclassified	